CHALMERS
UNIVERSITY OF TECHNOLOGY

Measurements of Sea Surface Currents in the Baltic Sea Region Using Spaceborne Along-Track InSAR

Citation for the original published paper (version of record):
Elyouncha, A., Eriksson, L., Romeiser, R. et al (2019). Measurements of Sea Surface Currents in the Baltic Sea Region Using Spaceborne Along-Track InSAR. IEEE Transactions on Geoscience and Remote Sensing, 57(11): 8584-8599. http://dx.doi.org/10.1109/TGRS.2019.2921705

(article starts on next page)

Measurements of Sea Surface Currents in the Baltic Sea Region using Spaceborne Along-Track InSAR

Anis Elyouncha, *Student Member, IEEE,* Leif E. B. Eriksson, *Member, IEEE,* Roland Romeiser, *Senior Member, IEEE,* and Lars M. H. Ulander, *Fellow, IEEE*

***Abstract*—The main challenging problems in ocean current retrieval from ATI-SAR are phase calibration and wave bias removal. In this paper, a method based on DInSAR technique for correcting the phase offset and its variation is proposed. The wave bias removal is assessed using two different Doppler models and two different wind sources. In addition to the wind provided by an atmospheric model, the wind speed used for wave correction in this work is extracted from the calibrated SAR backscatter. This demonstrates that current retrieval from ATI-SAR can be completed independently of atmospheric models. The retrieved currents, from four TanDEM-X acquisitions over the Öresund channel in the Baltic Sea, are compared to a regional ocean circulation model. It is shown that by applying the proposed phase correction and wave bias removal, a good agreement in spatial variation and current direction is achieved. The obtained *bias*, between the ocean model and the current retrievals, varies between 0.013 and 0.3 m/s depending on the Doppler model and wind source used for wave correction. This paper shows that using SAR as a source of wind speed improves the *bias* and *rmse* of the retrieved currents by 20 % and 15 % respectively. Finally, the sensitivity of the sea current retrieval to Doppler model and wind errors are discussed.**

***Index Terms*—Along-track interferometric SAR, Sea surface currents, Synthetic aperture radar, Doppler oceanography.**

I. Introduction

OCEAN surface currents play an important role in momentum, heat, gas and nutrients distribution which affects weather, climate and marine ecosystem. Understanding the dynamics of the upper ocean layer is of great importance for ocean circulation and climate modelling. Moreover, accurate measurements of ocean surface currents is a good support for marine navigation, pollution monitoring, coastal hazards management and ocean energy exploitation.

Synthetic Aperture Radar (SAR) has become a vital tool for ocean remote sensing mainly due to its day/night and quasi-all-weather capability and its high spatial resolution. These SAR capabilities are particularly useful in coastal and shelf seas where small scale processes dominate the upper ocean dynamics and where other sensors such as altimeters and scatterometers have limited usage. In these regions, ocean circulation is more complex and more spatially variable than in the open ocean due to a strong interactions with coastlines and bathymetry. Finally, coastal seas host many human and economic activities hence the relevance of their observation.

It is now relatively well understood how SAR detects the spatial structure of sea surface currents through modulation of the backscatter [1], [2] and how this affects the Doppler spectrum [3], [4]. However, retrieving the absolute value of the surface current from satellite data is still a challenging problem. This requires a high accuracy of the satellite orbital information (position, velocity and attitude), information on wind vectors, directional wave spectra and forward models able to simulate the radar response to the sea surface. Moreover, in SAR ocean remote sensing, airborne campaigns are generally carried out in collocation with in-situ measurements. Satellite observations are seldom collocated with oceanic in-situ data. Thus, most of the spaceborne SAR studies focused on oceanographic interpretation and qualitative comparisons of ocean currents, for demonstrating the capability of detecting currents spatial features such as fronts and eddies (e.g. [5]).

Along-Track Interferometric SAR (ATI-SAR) has demonstrated a unique capability to measure sea surface velocity. The first feasibility studies for measuring tidal ebb flows at the outlet of a bay were published by [6] and [7] using two L-band radar antennas separated in the flight direction and mounted on the aircraft fuselage. The capability of ATI-SAR in measuring surface velocity was confirmed through several other studies using airborne radars [3], [8]–[11]. The first study based on a space mission, exploiting the opportunistic along-track baseline in the Shuttle Radar Topography Mission (SRTM), was published by [12]. The first results using the divided antenna mode of TerraSAR-X were presented in [13]. The theoretical background and a numerical model for ATI-SAR was developed in [4]. The first studies based on the bistatic TanDEM-X formation were reported in [14], [15].

Along-track interferometry is based on two SAR acquisitions of the same area on the ground at two different times separated by few milliseconds. The pixel-by-pixel phase difference between the two complex focused SAR images is directly related to the Line-of-Sight (LOS), also called radial, velocity of the imaged surface patch. This is achieved either by using two antennas mounted on the same platform (this is mostly the case in airborne ATI) or by using two different platforms in tandem configuration (this is the case of the TanDEM-X formation).

A schematic of TanDEM-X acquisition geometry is illus-

A. Elyouncha is with the Department of Space Earth and Environment, Chalmers University of Technology, Gothenburg, SE-41296 (Sweden e-mail: anis.elyouncha@chalmers.se).

L. Eriksson is with the Department of Space Earth and Environment, Chalmers University of Technology, Gothenburg, SE-41296 (Sweden e-mail: leif.eriksson@chalmers.se).

R. Romeiser is with the department of Ocean Sciences, Rosenstiel School of Marine and Atmospheric Science, University of Miami, Miami, FL 33149 USA (email: rromeiser@rsmas.miami.edu).

L. Ulander is with the Department of Space Earth and Environment, Chalmers University of Technology, Gothenburg, SE-41296 (Sweden e-mail: lars.ulander@chalmers.se).

trated in figure 1. One difficulty in deriving ocean currents from hybrid (along- and across-track InSAR) systems such as TanDEM-X resides in its sensitivity to both surface elevation and motion. Moreover, differences in the two on-board channels, differences in the two satellites attitudes and time and phase synchronization between the transmitter and the receiver will induce an unknown phase offset. The requirement on the synchronization is even more stringent in bistatic mode [16].

In this paper, we present four acquisitions of the same geographical area, i.e. the Öresund, imaged at different times. In three acquisitions, the exact same area is imaged while in one acquisition the imaged area is shifted towards the north. The Öresund is an important channel for water exchange between the North Sea and the Baltic Sea. In general, the circulation in the Baltic Sea region is relatively weak (≤ 0.5 m/s), time varying and quasi-tidal free [17]. Shallow seas such as the Öresund is also highly affected by the bathymetry. This is a great challenge for the accuracy and precision of the satellite measurements and radar models.

Most of the previous ATI-SAR studies were carried out in areas with well defined and strong tidal currents (e.g., a strong tidal current at a bay's inlet/outlet) with velocities ≥ 1 m/s. Furthermore, few papers except [14], discussed the impact of the interferometric phase processing on the derived current velocity, the errors affecting current retrieval and quantified the absolute accuracy of these currents. Thus, we provide details of the phase processing and the impact of its correction on the derived radial velocity. The wave bias estimation and removal is one of the most difficult tasks in current retrieval. We assessed the wave removal using two different Doppler models (theoretical and empirical) and two different wind sources (atmospheric model and SAR). This is, to our knowledge, the first time that the estimation of the wave bias is based on the wind derived from the SAR backscatter. Finally, sources of error related to the Doppler model and wind vectors affecting the ocean current retrieval from ATI-SAR data are discussed.

This paper is organized as follows. First, the basic principles of SAR interferometry are reviewed in section II. Second, the test area and data set are described in section III. The interferometric phase processing is described in section IV. Section V is dedicated to phase calibration. This section describes how the topographic correction is performed using a Digital Elevation Model (DEM), and how the phase offset is estimated and removed from the topographic corrected phase. Section VI, describes the wave contribution (bias) to the surface velocity and how it is simulated and compensated using a Doppler model. The assessment of the Doppler model and wind vectors is discussed in section VII. The sensitivity of the currents retrieval to the Doppler model and wind errors is discussed in section VIII. Finally, a comparison of the derived surface currents with ocean circulation model data is presented in section IX, followed by a discussion of the results and conclusions.

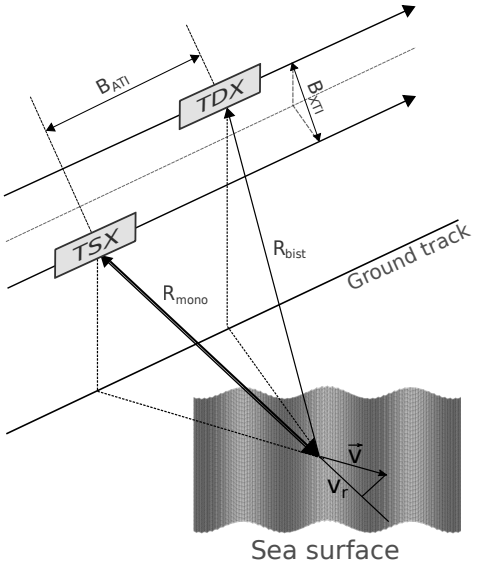

Fig. 1. Acquisition geometry of the bistatic and hybrid interferometric SAR, TanDEM-X. In this configuration, the master is TerraSAR-X and the slave is TanDEM-X. The B_{ATI} and B_{XTI} are the physical along-track and across-track baselines respectively.

II. Basic principles

A. Interferometric phase

The total phase measured by a bistatic and hybrid system such as TanDEM-X can be decomposed as

$$\phi = \phi_{topo} + \phi_{motion} + \phi_{atm} + \phi_{error} \tag{1}$$

where

$$\phi_{topo} = \frac{kB_{\perp}}{R\ \sin\theta} h \tag{2}$$

$$\phi_{motion} = \frac{kB_{ATI}}{V_{SAR}} v_r \tag{3}$$

$B_{\perp}$ and B_{ATI} are the perpendicular (to the LOS) and along-track baselines respectively, R is the slant range, θ is the incidence angle, $k(=2\pi/\lambda)$ is the wavenumber, h is the height relative to the ellipsoid, V_{SAR} is the satellite velocity, v_r is the radial velocity (the surface velocity projected on the LOS) and ϕ_{error} groups all the errors (systematic and random).

The atmospheric phase ϕ_{atm} in equation 1 contains the ionospheric and tropospheric delay difference. The ionospheric delay for X-band is negligible [18] and given the very small difference in time and incidence angle between the two acquisitions, the variation in the propagation delay is also negligible. Thus ϕ_{atm} will not be discussed further in the following.

From equation 3, the radial horizontal velocity (surface velocity projected on the ground range) v can be readily inverted

$$v = \frac{\phi_{motion}}{2\ k\ \Delta t\ \sin\theta} \tag{4}$$

Where $\Delta t(= B_{ATI}/2V_{SAR})$ is the time delay between the two acquisitions. In order to get ϕ_{motion}, which is of interest here, all the other terms in equation 1 should be estimated and removed.

B. Sensitivity and ambiguity

The sensitivity depends mainly on the along-track baseline (see equation 3). With a large baseline, a small variation in velocity yields a large variation in phase. On the other hand, a too large baseline might induce ambiguity. The ambiguity occurs when the phase difference induced by the surface velocity is $\phi_{motion} \geq 2\pi$. From equation 4, we get the horizontal Velocity-of-Ambiguity (VOA)

$$VOA = \frac{\lambda}{2\ \Delta t\ \sin\theta} \tag{5}$$

For example, our acquisitions (see table I) with $\Delta t = 2.5$ ms and $\theta = 30^o$, $VOA = 12.4$ m/s. Note that, since the phase is wrapped between $-\pi$ and π the velocity wraps between $-VOA/2$ and $VOA/2$. The ambiguity limited velocity is much higher than the expected sea surface velocities, i.e. it should not be exceeded by surface motion alone.

C. Correlation time

A long baseline increases the time delay between acquisitions. This time delay is constrained by the ocean decorrelation time, which depends on the radar wavelength and the standard deviation of the orbital velocity of the gravity waves σ_{orb} and can be approximated by [19]

$$\tau_{corr} = \frac{\lambda}{2\sqrt{2}\pi\sigma_{orb}} \tag{6}$$

For a given wind speed, the time between the two SAR acquisitions should not exceed the value given by equation 6. For instance, if we use the approximation $\sigma_{orb} = 0.068\ U_{10}$ [19], where U_{10} is the wind speed at 10 m height, we get, for $U_{10} = 10$ m/s and wavelength $\lambda = 0.031$ m, $\tau_{corr} = 5.13$ ms. Note that the data considered here are all acquired with time delays smaller than τ_{corr} as shown in table I.

III. Test area and DATA sets

A. Test area

The study area called the Öresund, shown in figure 2, is located in the south western part of the Baltic Sea, between Sweden and Denmark on its east and west sides respectively and between the Baltic proper and Kattegat basins on its south and north sides respectively. The Öresund channel is an important connection for the exchange of water masses between the Baltic Sea and the North Sea. The channel is shallow with a mean depth of 11 m and a sill of only 8 m depth (the Drogden Sill) at its southeastern inlet. The channel is approximately 100 km long and 10 km wide. There are four mechanisms responsible for the circulation in the Baltic Sea: surface wind stress, sea level variation, thermohaline density gradient and tides [17]. Moreover, currents are steered by Coriolis, topography and friction [17]. The tidal ranges are generally small in the order of few centimeters and the density driven current is slow hence only important in long time scales. On short time scale (1-5 days) the wind stress and sea level are the most relevant mechanisms. Furthermore, it is often assumed [20]–[22] that the flow in the Öresund is mainly driven by the air pressure difference between the North Sea and Baltic Sea and the sea level gradient between the Kattegat and the Baltic basins.

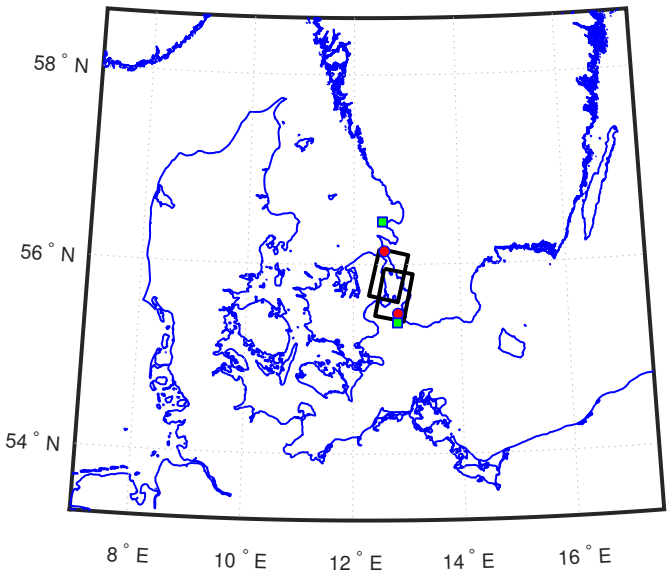

Fig. 2. The geographical location of the test area: the Öresund. The two black rectangles outline the SAR images, bottom: acquisitions 1, 2 and 4, top: acquisition 3. The locations of the SMHI stations are plotted as green squares for wind (top: Hallands Väderö, bottom: Falsterbo) and as red circles for the sea level (top: Viken, bottom: Skanör).

B. Satellite SAR data

All the satellite data used in this paper are provided by the TanDEM-X formation [16]. The primary application of the TanDEM-X mission is the generation of a global DEM. TerraSAR-X and TanDEM-X are two identical satellites flying in close formation and carrying identical SAR instruments operating at X-band ($f = 9.65$ GHz). The data used in this study, called Co-registered Single-look Slant-range Complex Products (CoSSCs), are pre-processed for interferometry by the German Aerospace Center (DLR). These images are all acquired in descending pass (heading$\approx 190^o$ w.r.t North), VV polarization, stripmap and Single Receive Antenna (SRA) mode with the antenna looking to the right of the flight direction.

In all the images the master (active transmitter) is TerraSAR-X (TSX) and the slave (bistatic receiver) is TanDEM-X (TDX). Also, the master is lagging / leading the slave in along and across track directions respectively as shown in figure 1, hence the negative along-track and positive across-track baselines in table I. The main criteria for the data selection are the along-track baseline and the coherence, which determines the sensitivity and phase noise respectively. A long baseline provides high sensitivity to velocity, on the other hand, if it is too long the coherence decreases. A compromise between these two quantities yields $10 < B_{ATI} < 50$ m [4], [16], [23]. The other criteria are that images should contain land for phase calibration (see section V), and should be located within the domain of the used ocean circulation model. A small across-track baseline or equivalently a large Height-Of-Ambiguity (HOA), to mitigate sensitivity to topography and avoid occurrence of phase wrapping, is also preferred. Table I summarizes the most relevant parameters of the acquisitions.

TABLE I
ATI-SAR ACQUISITIONS AND PARAMETERS

Acquis. #	Date/Time UTC	Incidence angle (^{o})	B_{ATI} (m)	Time delay (ms)	B_{XTI} (m)	HOA (m)
1	2014-08-09 05:33:26	33.28	-19.72	2.6	23.50	-222.5
2	2014-08-20 05:33:26	33.29	-19.46	2.5	22.69	-230.5
3	2014-09-05 05:41:57	21.55	-19.11	2.5	5.29	-1965.6
4	2014-09-11 05:33:27	33.24	-18.43	2.39	23.23	-225.2

TABLE II
WIND SPEED AND DIRECTION FROM DMI-HIRLAM MODEL AND CURRENT SPEED FROM HBM MODEL

Acquis. #	wind speed average	wind direction w.r.t North	SAR wind speed	current speed average
1	5.98 m/s	120 deg (S-E)	5.67 m/s	0.30 m/s
2	10.69 m/s	248 deg (S-W)	9.25 m/s	0.50 m/s
3	5.16 m/s	95 deg (S-E)	5.02 m/s	0.27 m/s
4	6.33 m/s	52 deg (N-E)	4.09 m/s	0.16 m/s

C. Ocean model data

The ocean currents model data are provided by the Danish Meteorological Institute (DMI) based on the HIROMB-BOOS-Model (HBM) [24]. HIROMB is an abbreviation for High Resolution Oceanographic Model for the Baltic and BOOS stands for the Baltic Operational Oceanographic System. HBM is a regional 3D ocean circulation model covering the Baltic Sea and the North Sea. The data used here are from a two-way nested high-spatial-resolution domain, called transition area. This model domain covers the Kattegat and a part of the southern Baltic Sea. The model outputs have been validated against current observations in the Baltic Sea [25]. The reported accuracy of the HBM surface (-5<depth<0 m) currents is ≈ 0.14 m/s [25]. The horizontal spatial resolution of the ocean currents is 0.5 nautical miles and the vertical top layer thickness is 2 m. HBM is forced by DMI's numerical weather prediction model DMI-HIRLAM with a 3 km grid size of the wind field. The DMI-HIRLAM wind fields are depicted in figure 3 (top row) for our study cases. The colour map is the radial component of the wind and the arrows represent the wind vectors. The average wind speed, direction and current speed for the four acquisitions are provided in table II.

D. In-situ data

No in-situ current measurements were found in the area of interest, that were collocated in time and space with available satellite images. Wind measurements were available from two Swedish Meteorological and Hydrological Institute (SMHI) weather stations called Falsterbo and Hallands Väderö. The first station is located close to south eastern corner of the study area while the second one is located slightly out of the study area toward the north . These in-situ wind measurements are used for the assessment of the atmospheric model DMI-HIRLAM and the SAR derived winds. Sea Level measurements were also available from two SMHI tide gauges Viken and Skanör. These measurements are used for the interpretation of the current fields and are discussed further in section IX. The locations of the four SMHI stations are depicted in figure 2 with the test area.

E. DEM

The DEM used in this study is a product of the Shuttle Radar Topography Mission (SRTM) with a spatial resolution of 3 arcsec (0.000833 deg lon/lat or $\sim$90 m). These data are freely available on (https://lta.cr.usgs.gov/SRTM). The original SRTM DEM is referenced to the EGM96 geoid. For our purpose it is converted to WGS84 ellipsoid referenced heights.

IV. INSAR PROCESSING

The input to the InSAR processing chain is the CoSSC products [26]. These data are generated and pre-processed by DLR for interferometric applications. The pre-processing consists mainly of focusing the two SAR images, coregistration and common band spectral filtering in range and azimuth. As mentioned above the phase unwrapping is usually not needed given the short along-track baselines, the large HOA and slow sea surface velocities. In some rare cases, phase wrapping may occur but is generally not of geophysical origin alone but rather due to a calibration offset which adds to the geophysical phase. Thus phase unwrapping is not discussed in this paper.

A. Interferogram formation

The interferogram is computed as the sample mean of the complex correlation of the master (TSX) and the slave (TDX) Single Look Complex (SLC) images [27]

$$\gamma = \frac{E\{s_1 s_2*\}}{\sqrt{E\{|s_1|^2\}E\{|s_2|^2\}}} \tag{7}$$

where E is the expectation operator. It is replaced by spatial averaging assuming that the phase is stationary and ergodic in a small area around the pixel of interest. In this study, 55×54 pixels are averaged into one pixel. The spatial resolution is downgraded from 0.91×1.85 m, in slant range and azimuth respectively, to ≈100×100 m horizontal resolution. The interferometric phase is defined as the argument of γ

$$\phi = arg\{\gamma\} \tag{8}$$

B. Coherence and phase noise

The coherence is defined as the magnitude of γ and is an essential indicator of the quality of the phase and hence the interferometric performance. The phase/velocity precision depends mainly on the interferometric coherence. Since common band filtering was applied to the data used here, we assume that the geometric decorrelation is negligible. Thus, the main sources of decorrelation are thermal noise (SNR) and temporal decorrelation. The Cramer-Rao Bound (CRB) of the interferometric phase is given by [27]

$$\sigma_\phi^2 = \frac{1-|\gamma|^2}{2N|\gamma|^2} \tag{9}$$

where N is the number of independent averaged samples.

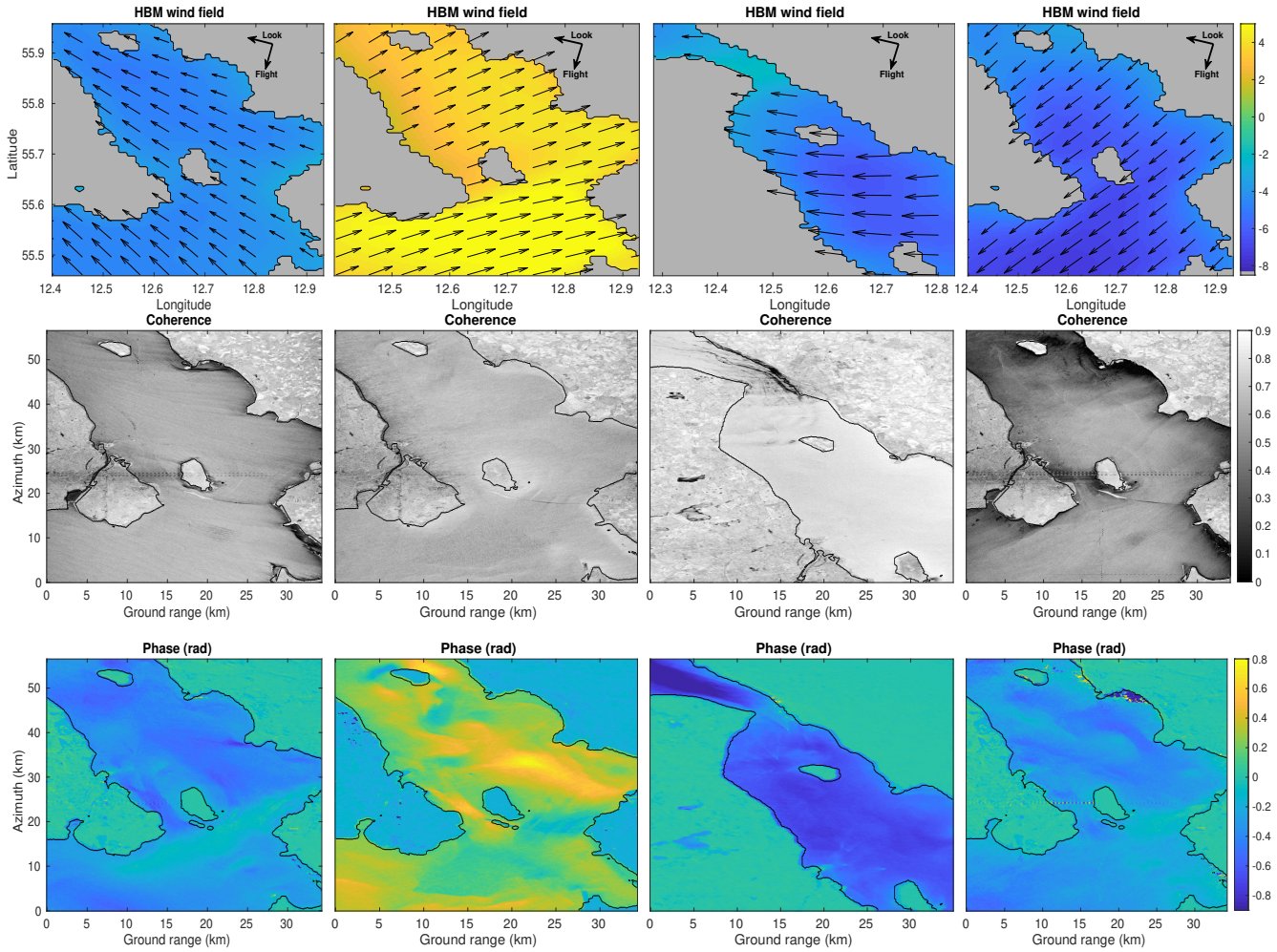

Fig. 3. Top row: DMI-HIRLAM wind field at 10 m height; the colour map represents the radial wind (wind vector projected on the radar LOS) and the arrows represent the wind vectors; the grey areas are land; the flight and look directions of the satellite are indicated on the figure with the black arrows. Middle row: the estimated coherence from TanDEM-X CoSSC data; Bottom row: calibrated phase from TanDEM-X CoSSC data; first col: acquisition 2014-08-09, second col: acquisition 2014-08-20, third col: acquisition 2014-09-05, fourth col: acquisition 2014-09-11.

Equation 9 shows that the lower the coherence the larger is the phase variance, the more samples need to be averaged to reduce the variance. As an example, a coherence $\gamma = 0.5$ (over sea) and $N = 2970$ averaged samples, yields $\sigma_\phi \approx 0.022$ rad and with $V_{sat} = 7.68$ km/s and $B_{ATI} = 20$ m, the ground velocity standard deviation is $\sigma_v \approx 0.04$ m/s. Note that these are the lowest theoretical standard deviations. In this calculation, uncertainties in B_{ATI} and V_{SAR}, were neglected. Furthermore, the averaged samples are not effectively independent due to the fact that the pixel size is slightly smaller than the effective resolution and due to the weighting window (applied with overlapping) before ATI processing. Thus, in practice, the actual value for the velocity standard deviation σ_v is likely larger.

Figure 3 (middle row) shows the coherence for the four study cases. It can be noted that the coherence, over sea, is generally correlated to the wind (top row), i.e. areas with strong wind have higher coherence and areas in the wind shadow have lower coherence. This is mainly because the SNR, over ocean, is dependent on wind speed, direction, and incidence angle. The streak, visible in image 1 and 4, extending in the range direction over the southern island is probably due to a radio interference. Note that acquisition 2014-09-05 (image 3) has the smallest incidence angle (21^o), hence the high coherence/SNR over all the image including land. This indicates that the main contribution to the loss of coherence, for a given B_{ATI}, is the SNR.

Finally, the bottom row of figure 3 depicts the calibrated phase of each acquisition. It can be observed that the phase follows the radial wind (top row), i.e. positive in upwind and negative in downwind, which indicates that the ATI-SAR phase is dominated by the wind. This is discussed in further details in the following.

C. Phase simulation

Phase simulation is needed for topographic phase removal. The phase is simulated using equation 2. The simulated interferogram $\gamma_{sim} = e^{j\phi_{sim}}$ is removed from the measured interferogram by complex multiplication $\gamma.\gamma^*_{sim}$. Note that phase simulation is based on the annotated satellite state vectors, thus also affected by orbit inaccuracies. This is generally manifested as a quasi-linear signal in the interferometric

TABLE III
PHASE AND VELOCITY STANDARD DEVIATION (SD). THE PHASE SD IS ESTIMATED OVER LAND AFTER CALIBRATION. THE VELOCITY SD IS CONVERTED USING EQUATION 4.

Acquis. date	2014-08-09	2014-08-20	2014-09-05	2014-09-11
Phase SD (rad)	0.06	0.07	0.057	0.058
Velocity SD (m/s)	0.10	0.12	0.15	0.10

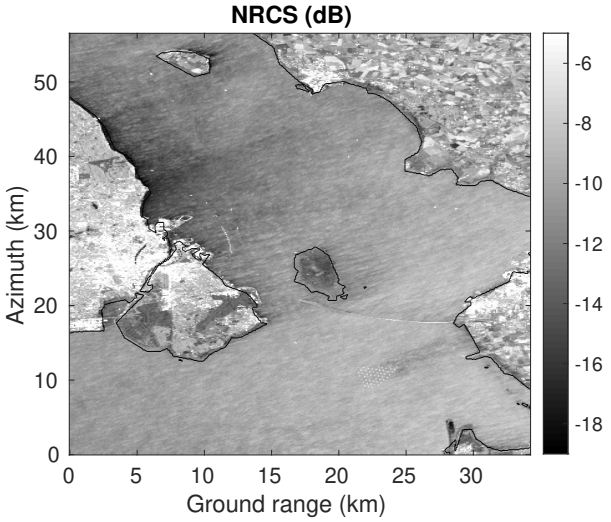

Fig. 4. The Normalised Radar Cross Section (NRCS) in dB, measured by TerraSAR-X over the Öresund, acquisition 2014-08-20.

phase [18]. This signal is almost inevitable and needs to be corrected in a post-processing step (see section V).

V. PHASE CALIBRATION

The objective of the interferometric phase calibration is to estimate and correct systematic errors, which directly affect the sea surface velocity retrieval accuracy. Systematic errors may be caused by residual phase offsets in the instrument electronics or by inaccuracies in satellite state vectors.

The estimated interferometric phase can be expressed as

$$\phi = \phi_0 + \overline{\phi}_{error} + \tilde{\phi}_{error} \tag{10}$$

Where ϕ_0 is the true value of the phase (the geophysical phase) and the phase error ϕ_{error} is decomposed into a systematic mean offset (bias) $\overline{\phi}_{error}$ and a fluctuating (random) component $\tilde{\phi}_{error}$.

In order to retrieve the absolute surface velocity, a phase (or velocity) calibration has to be performed by determining and subtracting $\overline{\phi}_{error}$. The fluctuation term can be reduced by spatial averaging. If the measured phase is directly converted into velocity without any correction, a non-zero velocity is systematically obtained over land and unrealistic velocities are obtained over sea. This was the case of all images processed for this study and it was also observed in [13].

Phase calibration requires a reference (in height and/or velocity) for which the phase can be predicted. The most common approach is using a flat ($h = 0$) and static ($v_r = 0$) target, e.g. coastline. This approach requires an area of negligible height in the image. Due to topography, the flat land area (if it exists) is usually limited to a few pixels. Moreover, since the phase offset usually varies along and/or across-track (see figure 5), this approach might provide a biased estimate of the mean offset value depending on the location of the flat pixels.

Two authors, [28] and [29], explored an approach which consists of using moving ships with known velocity to calibrate the ATI phase in open ocean where land is not imaged. First, this is not valid for ships moving in the along-track direction. Second, due to the SAR imaging principle (assumes static targets for focusing), the smearing of the ship's signature in the SAR image over several pixels introduces large uncertainties in the estimated ship velocity, which makes this approach of limited use.

Other authors used a geophysical plausibility approach. For example [12], in analysis of the Wadden Sea data, the calibration was based on the criterion that radial velocity at the IJsselmeer dam, which is oriented almost perpendicular to the radar look direction, must be close to zero. The same approach was adopted in another case [23] of the Elbe River. The fact that orientation of the river boundaries with respect to the radar look direction varies by almost 90^o within the image was exploited. Similarly, in [14] the current velocities were calibrated to satisfy the condition of zero mean currents at coastlines perpendicular to the radar look direction.

In this paper we adopt a different approach. A DEM is used to simulate the phase induced by the topography, since high resolution and accurate DEMs are now available for many areas. This is similar to the two-pass Differential InSAR (DInSAR) technique [30] for estimating land displacement although the objective is different. First, note that in contrast to the monostatic systems used for DInSAR, a bistatic system is used here, which is more prone to phase errors. Moreover, here we flatten the land phase in order to estimate a calibration mean offset. The mean offset is computed as a coherence weighted average of all land pixels. The estimated offset is applied to the phase over ocean assuming that this offset is instrumental, orbital and geometrical rather than geophysical. This is based on the fact that the variance of sample mean of a random variable is inversely proportional to the number of samples. Thus, exploiting all available land pixels will improve the accuracy of the $\overline{\phi}_{error}$ estimate, i.e. the sample mean approaches the expected value.

After topographic phase removal the obtained phase over land is randomly distributed around a mean ($\overline{\phi}_{error}$). This allows the estimation of the phase standard deviation ($\tilde{\phi}_{error}$) which is important for performance assessment. The estimated phase standard deviation for all acquisitions is reported in table III. This is the limit of the current retrieval precision using this method at this spatial resolution (≈100 m). Note that the $\overline{\phi}_{error}$ now includes possible DEM errors used for topographic correction. As mentioned above, there is a slight trend in the phase in range and azimuth directions, only the range trend is shown in figure 5. This trend is modelled by a 2D quadratic polynomial and removed from the total phase. Detrending is only possible if the land extends sufficiently over the image. Over ocean, one can not distinguish between a geophysical trend and a geometric trend. The calibrated phases for the four acquisitions are depicted in figure 3 (bottom row).

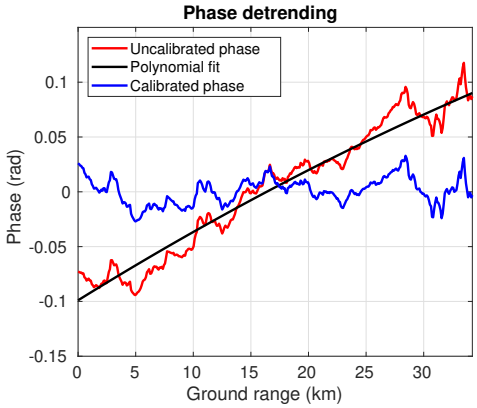

Fig. 5. Phase calibration for the acquisition 2014-09-05; the correction of the phase offset and ramp in range direction, red curve: before correction, blue curve: after correction.

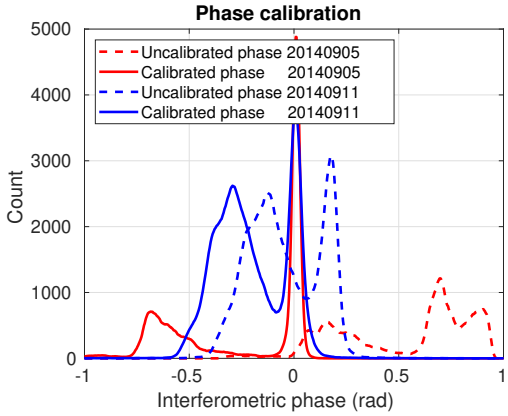

Fig. 6. Histogram of the interferometric phase before and after phase calibration for the acquisitions 2014-09-05 and 2014-09-11; dashed line: before calibration, solid line: after calibration. Only two study cases are plotted for clarity.

It can be observed that the phase over land is uniform with zero average and the phase over sea varies with wind and currents. Finally, figure 6 depicts the phase distribution before and after calibration, for two acquisitions, to illustrate how the distribution is affected by calibration. The two modes of the phase distribution represent the land and sea. Note that the land peak is shifted to zero and becomes much narrower after calibration due to the detrending.

VI. Wind-wave removal

In principle, ATI-SAR measures the total radial velocity due to the motion of the surface roughness. This motion includes all types of currents (sea level driven, wind driven, density driven, tides and river runoff) and all type of waves (surface wind-waves, swell and internal waves). For our test area (the Öresund), the density driven currents are generally much slower than the wind driven currents [31]. The contributions of density driven currents, tidal currents and swell are assumed to be small [17]. Thus, it is expected that the main contributions to the surface motion include wind-induced drift (Ekman current + Stokes drift), wind-waves and geostrophic currents. The barotropic flow driven by sea level variation between the North Sea and the Baltic Sea [17], [20] is often considered as the dominant driver for the circulation in the Danish belts and the Öresund channel [21], [31].

A. Wave bias

Thompson has shown [32], [33] that the motion of long gravity waves (few times longer than Bragg waves), not only broadens the Bragg spectral lines but also causes a shift in the peak of the Doppler spectrum deviating this peak from the Bragg frequency. It has also been shown [3], [8] that the ATI-SAR phase is proportional to the mean Doppler frequency for short time delays. Therefore, it can be assumed that the ATI-SAR phase is affected in the same way, by the long waves, as the Doppler spectrum peak. The effect of wave motion on Doppler shift has been investigated in several papers [4], [8], [33]–[36]. It is now well established, theoretically and experimentally, that even in the absence of currents a wave induced Doppler shift is measured. This Doppler shift does not correspond to water mass transport (current) thus it needs to be removed from the total phase. Models predicting this wave-induced Doppler shift are needed for this purpose.

The ATI-SAR phase measures the ocean motion, which includes phase velocity of the Bragg waves, the orbital velocity of the long waves and ocean surface currents (the quantity we want to retrieve). These contributions are illustrated schematically in figure 7 and can be expressed as

$$U_r = U_{Bragg} + U_{orbital} + U_L \tag{11}$$

Where U_r is the total velocity (converted from the calibrated phase), U_{Bragg} is the Bragg wave phase speed, $U_{orbital}$ is the orbital velocity of the long gravity waves. All these contributions refer to the projection onto the line of sight. The total Lagrangian current U_L can be decomposed as the sum of a quasi-Eulerian current [37] U_c and the Stokes drift U_{Stokes} at the sea surface [34], [38]

$$U_L = U_{Stokes} + U_c \tag{12}$$

U_c is the quantity measured by fixed sensors such as Acoustic Doppler Current Profilers (ADCP). There is a debate about whether radars measure the Stokes drift or not and how much it contributes to the total velocity [39], but this is out of the scope of this paper.

Very often the wind-wave bias ($U_{Bragg}+U_{orbital}$) is higher than the proper current contribution thus dominating the ATI-SAR phase response to ocean motion. For instance, note that the sign of the phase images shown in figure 3 (bottom row) correspond to the wind direction, i.e. positive for the second image and negative for the other images. This reflects the quasi upwind/downwind situations (see figure 3, top row), whereas the currents vary in direction, which suggests the domination of the wind-wave bias to the phase. Note also that the magnitude of the wind-wave bias is wind direction dependent being maximum in the upwind/downwind direction and minimum in crosswind direction as illustrated in figure 8. In all our study cases the wind is quasi up-/downwind, while the currents (shown later) are quasi cross the look direction, which is even more favourable to the wave motion dominance.

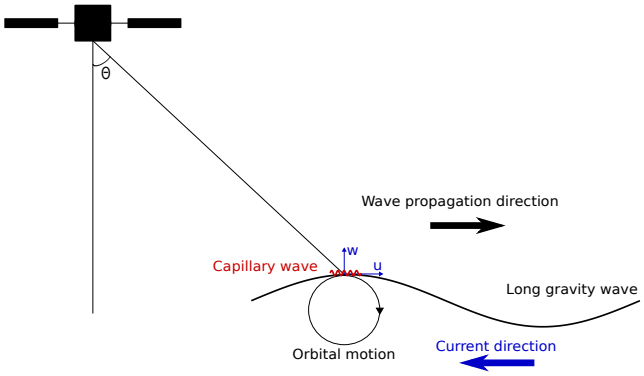

Fig. 7. Illustration of different contributions to ocean surface motion and to ATI-SAR phase: Bragg (capillary) waves, orbital velocity of long gravity waves and current. The Stokes drift also contributes, but is not illustrated in this figure. Adapted from [34].

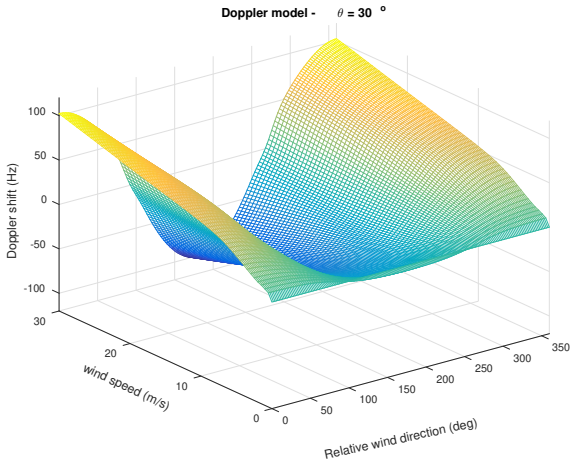

Fig. 8. The Doppler model, used for wave bias removal, as a function of wind speed and wind direction relative to the antenna look for incidence angle $\theta = 30^o$.

Calculation of the Doppler shift induced by the orbital velocities of long waves is a complicated task. This is because the orbital velocities are weighted by the Radar Cross Section (RCS), which varies along the long waves profile due to tilt and hydrodynamic modulation [4], [8], [33], [34], [40]. Thus, this calculation requires a RCS model and a model for the wave spectrum. For the Bragg waves, the phase speed can be calculated from the dispersion relation, which yields $\sim$ 24 cm/s for X-band. The Stokes drift is also complicated to calculate and it requires a wave spectrum model. According to reported results, it is in the order of 1.5% of the wind speed U_{10} [38], [41].

B. The Doppler model

The Doppler model refers, here, to a model relating the Doppler shift as measured by the radar to the sea surface wind speed and direction. Such a model is parametrized by the instrument configuration (frequency, polarization and incidence angle). The modelling of how the radar images surface currents via the modulation of current gradients of the wave spectrum and its effect on the Doppler spectrum was studied in several papers with different approaches. The first approach is by developing a time-dependent RCS model from which the Fourier transform of its covariance matrix yields a Doppler spectrum [32], [42]–[44]. The second approach is by using a Doppler Modulation Transfer Function (MTF) based on wave orbital velocity and wave spectrum [4], [40], [45], [46]. The second approach is usually faster.

Few available Doppler models are capable of relating the radar Doppler shift to the sea surface wind field particularly at X-band. To our knowledge, there is no empirical Doppler model at X-band similar to CDOP for C-band [42]. Theoretical models are proposed in [4] and [40]. In this paper, the numerical model called M4S presented in [4] is used. A Look-Up-Table was created from the M4S model for C-band ($f = 5.4$ GHz) and X-band ($f = 9.65$ GHz), called hereafter DOPLUT-C and DOPLUT-X. The Doppler shift is simulated for incidence angle, wind speed and wind direction ranges $[20 - 50^o]$, $[0 - 30]$ m/s and $[0 - 360^o]$ respectively. The simulation is performed using the equilibrium wave spectrum described in [47] with zero currents. A 3D plot of the DOPLUT-X is depicted in figure 8 as a function of wind speed and relative direction. For comparison, the C-band empirical model CDOP [48] and its scaled version to X-band, called here CDOP-X, is also used. This is discussed further in section VIII-A. The scaling factor (p) is the ratio of wavelength at X-band and C-band $p = f_X/f_C$, where ($f_X = 9.65$ GHz and $f_C = 5.4$ GHz). The scaling is done by multiplying the Doppler frequency value obtained from CDOP by the scaling factor, i.e. $f_{CDOPX} = p \times f_{CDOP}$. Similar scaling has been done for Ku-band in [49].

In contrast to [40], the MTF adopted by M4S model does not take into account breaking waves. It has been shown that wave breaking has a noticeable effect on the radar backscatter [50], hence it consequently affects the radar Doppler spectrum. A RCS model called Radar Imaging Model (RIM) was developed to take into account this effect. This model was extended by [40] to produce a radar Doppler model called (DopRIM). It was proven that RIM was capable of simulating the modulation of RCS by current variation due, for instance, to internal waves, eddies and oceanic fronts [1], [2]. This was further assessed against ENVISAT/ASAR data in [51]. Note however that the wave breaking effect is much more important in HH polarisation and at higher incidence angles than in VV polarisation and lower incidence angles respectively [52]. Thus, the effect of wave breaking is neglected in this study.

C. Wind speed retrieval

In order to estimate the wave bias (see section VI), the wind speed and direction are needed. Thus, the accuracy of the wind vectors have a direct impact on the current retrievals. The wind vectors provided by the DMI-HIRLAM model are the same wind vectors used for the forcing of the ocean model. Our current retrievals are compared to the HBM ocean model used as a reference here. Thus, in order to be completely independent of the ocean model, the wind speed is derived from the TerraSAR-X calibrated NRCS. This allows us to test the effect of using different wind sources, i.e. model and SAR. This also demonstrates that current retrieval can be performed

independently of atmospheric models in some cases. Since the wind direction is quasi uniform over the whole scene (see figure 3), it is obtained from nearby weather stations. Also, wind direction can be retrieved from the SAR image using wind streak directions [53], [54], but this is not done here. In this study, the wind speed is retrieved by inversion of the Geophysical Model Function (GMF) XMOD2 [55]. The NRCS is calibrated using the calibration and noise factors provided by DLR in the auxiliary files. An example of the calibrated NRCS of the second acquisition is depicted in figure 4, which shows that wind signatures (wind streaks and shadowing) dominate the backscattering (see figure 3 for model wind vectors). The average retrieved wind speed is reported in table II. Note finally that the SAR NRCS is a measure of wind stress which is affected by surface currents. However, current magnitude in our area is weak compared to the wind ($< 3\%$) and the direction of the wind and currents are quasi orthogonal yielding a minimum interaction. Thus, the effect of the currents on the wind retrieval is negligible.

D. Wave bias removal

For removing the wave bias, the Doppler model described above and wind information are required. The winds are obtained from an atmospheric model or retrieved from SAR backscatter as described above. We neglect the wave spectrum modulation due to wave-current interaction. The wave-current interaction requires solving the wave action balance equation for each grid point and that is very time consuming. The main underlying assumption is that the advection effect of the currents on the waves is more important than the modulation of the wave spectrum by the currents. This assumption is based, first, on the experience of other authors [4], [11], [14], [56] and, second, on the following arguments specific to this work. The wave spectrum is modulated by the current gradient due to convergence/divergence and this effect decreases with frequency, thus it is expected to be small at X-band [3], [4], [32]. Moreover, in our study cases, the current direction (North-South) and the wave direction (East-West) should lead to the minimum of the hydrodynamic modulation [4]. In addition, the current gradients are relatively small and no clearly visible modulation in the backscatter image in figure 4. By visual inspection of the backscatter and phase images (figures 3 (bottom row) and 4), it can be observed that the NRCS, in contrast to phase, is dominated by wind variation rather than current gradients. Therefore, given all these elements, this assumption is reasonable.

Few authors [10], [11], [56] have attempted wave bias removal based on a radar Doppler model. In [10], iterative runs of the M4S model, accounting for all effects, have been used to correct the wave Doppler velocities. In [56] the CDOP is used to correct Sentinel-1A radial velocity. In [11] the CDOP model was also used to remove the wave bias although the data were acquired by an airborne X-band radar. They assumed that CDOP could be applied to X-band, although the authors found differences between CDOP and their data. Figure 9 depicts the variation of the two Doppler models as a function of incidence angle, wind speed and direction. The figure shows that the difference between DOPLUT and CDOP depends on wind speed, incidence angle and wind direction. The wind speed in [11] is $\sim$5 m/s where the difference is small. This might explain why their correction worked reasonably well, which is not valid for all wind conditions and incidence angles.

In this paper, we assess the wave correction using two Doppler models, i.e. the DOPLUT-X and the scaled CDOP and two wind sources, i.e. DMI-HIRLAM and SAR. The Doppler model, fed with wind, is used to calculate the wave-induced Doppler shift, which is converted to radial velocity, and removed from the total radial velocity by subtraction

$$U_c = U_r - DOPLUT(\theta, U_{10}, \phi_w) \tag{13}$$

where θ is the incidence angle, U_{10} the wind speed and ϕ_w the wind direction relative to the antenna look direction.

VII. Doppler model and wind assessment

A. Doppler model assessment

Since the necessary wind-wave bias removal step for deriving ocean currents involves the Doppler model, it is essential to assess its validity against for instance other models. As mentioned above, the Doppler model depends on a RCS model and on wave spectrum. It has been shown that simulations of the Doppler spectrum using different RCS models and different wave spectra may lead to relatively large differences in Doppler shifts [33], [42], [43]. We compared (not shown here) the M4S model using Romeiser's [47] and Elfouhaily's [57] wave spectra and we found relatively large differences both in RCS and Doppler shift. The best agreement in RCS with the empirical model XMOD2 is obtained using the Elfouhaily's spectrum. Conversely, the best agreement in Doppler shift against CDOP was obtained using Romeiser's spectrum. Thus, for the construction of DOPLUT, discussed above, we decided to use the wave spectrum and tuning parameters (e.g. directional spreading function) that produces the results closest to CDOP at C-band and the same parameters were selected for X-band.

We also compared the CDOP empirical model and the DOPLUT-C (see figure 9). The two models reproduce similar functional form with different parameters, i.e. decreasing with increasing incidence angle, increasing with wind speed and similar variation with direction. Differences up to 10 Hz were however found between the two models. These differences vary with incidence angle, wind speed and direction, but in general there is a slight negative offset of M4S against CDOP. The curve of DOPLUT-X is also shown in figure 9 together with a scaled version of CDOP. It also follows very similar functional form as CDOP-X with lower Doppler shifts. Compared to theoretical figures provided in [42], [43], DOPLUT-X overestimates the Doppler shift by approximately 10-20 Hz. To summarise, DOPLUT-C underestimates the Doppler shift w.r.t CDOP and DOPLUT-X overestimates it w.r.t to CDOP-X and [43], i.e. the bias is not consistent. Without supporting data we are not able to validate, nor to correct the absolute Doppler values of the DOPLUT-X. This is left for future work.

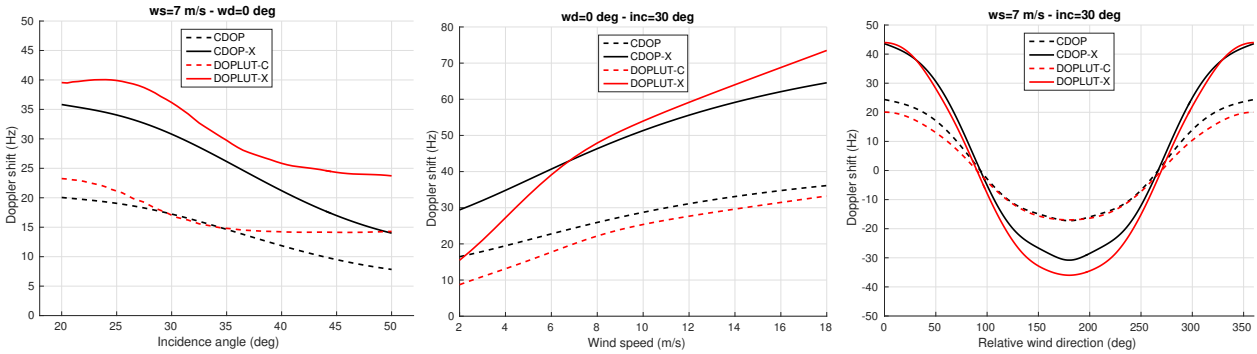

Fig. 9. Doppler shift simulated using DOPLUT-C, CDOP, CDOP-X and DOPLUT-X as a function of incidence angle, wind speed and relative wind direction from left to right respectively. CDOP-X is a scaled version of CDOP, the scaling factor is the ratio of wavelength (λ_X/λ_C).

B. DMI-HIRLAM model wind assessment

The purpose of this assessment is to investigate any systematic bias between the model wind and the in-situ data. This bias would be used to correct the wind input to the Doppler model in order to estimate the wave bias. It is also meant to investigate any dependence of the bias on wind speed or direction. For comparison with the model wind speed, the measured wind speed, at Falsterbo station, was corrected for height using a logarithmic profile and assuming neutral stability with a roughness length $z_0 = 2.10^{-4}$. The time series over 24 hours of the atmospheric model and SMHI stations (not shown) follow roughly the same trend but they can differ by several m/s at certain times. The errors between DMI-HIRLAM and SMHI weather stations of wind speed and wind direction corresponding to the four study cases are depicted in figure 10. The mean bias and RMSE values are calculated over a period of 24 hours around the satellite acquisition time for each study case. The instantaneous maximum difference can be as large as 3 m/s and 35 deg in wind speed and direction respectively. However, no systematic bias has been detected. The deviations, though sometimes large, are arbitrary and within the RMSE. In addition, no clear dependence on wind speed or on wind direction is observed. The average RMSE over the four acquisitions and the two stations is 1.59 m/s.

VIII. Velocity retrieval sensitivity to errors

In addition to the uncertainty induced by the phase noise reported in table III, which refers to the velocity error before wave bias removal, current retrieval will also be affected by errors in the Doppler model and the wind vectors.

A. Doppler model error

The accuracy of ocean current retrieval is directly dependent on the Doppler model used for wave bias estimation. For C-band, based on Envisat/ASAR data, the reported errors are ∼5-7.5 Hz [48], [58]. Following the assessment in section VII, the mean bias between DOPLUT-C and CDOP and between DOPLUT-X and CDOP-X has roughly the same magnitude (∼5-10 Hz). The derivation of the empirical uncertainty of DOPLUT-X requires a validation against a large amount of X-band calibrated data, similar to what has been done in [58] and [48]. If we assume that similar errors apply to X-band, a Doppler model error of 7 Hz, at 30^o incidence angle, this is equivalent to 0.2 m/s error in ground range velocity which is not negligible. To achieve a 0.1 m/s velocity accuracy, an error less than 3.2 Hz is required at the same incidence angle.

B. Wind error

The current retrieval accuracy is also dependent on the wind vectors accuracy via the wind-wave bias removal. Since the wave bias removal, as adopted here, is a linear operation (see equation 13), the sensitivity of the retrieved current is directly related to the sensitivity of the Doppler model to wind speed. This sensitivity varies with incidence angle, wind speed and direction, but we limit our assessment to one incidence angle and wind direction for simplicity. In order to evaluate the contribution of the wind error to the simulated surface velocity, the sensitivity of the model to wind speed is calculated and depicted in figure 11. It can be noticed that the sensitivity of the Doppler velocity varies between 0.2 and 0.08 m/s for wind speeds between 2 and 10 m/s. The standard reported wind speed accuracy from scatterometry (e.g. [59]) is $1 < \sigma_{U_{10}} < 2$ m/s. This agrees with the accuracy (1.59 m/s) estimated from our comparison of DMI-HIRLAM and in-situ wind measurements (see section VII-B).

The wind error contribution to the velocity error, via the Doppler model used to estimate the wave bias, is expressed as follows

$$\sigma_{U_{DOP}|U_{10}} = \left|\frac{\partial U_{DOP}}{\partial U_{10}}\right| \sigma_{U_{10}} \tag{14}$$

Where $\sigma_{U_{DOP}|U_{10}}$ is the Doppler velocity error, given a wind speed, due to wind error and $\sigma_{U_{10}}$ is the standard deviation of the wind speed at 10 m. Using equation 14 with the sensitivity from figure 11 and $\sigma_{U_{10}} = 1.6$ m/s, this yields velocity error between 0.1 and 0.3 m/s. To achieve 0.1 m/s velocity accuracy, a $\sigma_{U_{10}} \leq 1$ m/s is required.

IX. Results and discussion

A. Comparison of ATI-SAR currents against the HBM model

In all processed interferograms, the ATI phase after topographic removal, exhibits a non-zero and spatially varying offset over land. Thus, phase calibration, as described in

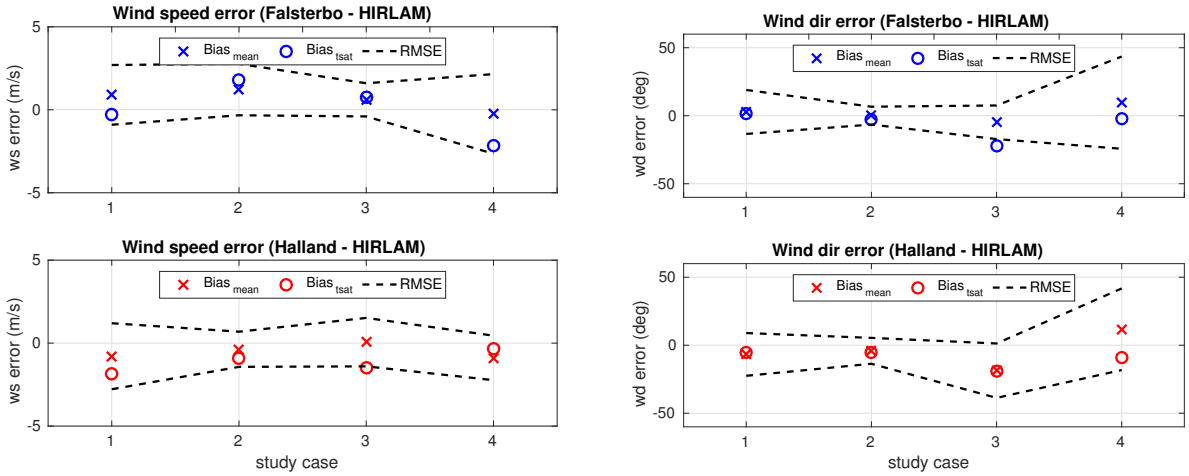

Fig. 10. Comparison of wind speed (left) and direction (right) measured by SMHI wind stations Falsterbo and Hallands Väderö and the DMI-HIRLAM atmospheric model; For Falsterbo the wind speed is corrected for height from $h = 5$ m to $h = 10$ m. The mean wind speed RMSE is 1.7 m/s and 1.46 m/s for Falsterbo and Hallands Väderö respectively. The mean wind direction RMSE is 17.75 ^{o} and 14.08 ^{o} for Falsterbo and Hallands Väderö respectively. The Bias$_{mean}$ and RMSE are calculated over 24 hours and Bias$_{tsat}$ is the instantaneous bias at the time of the satellite acquisition.

TABLE IV
RESULTS OF THE COMPARISON OF THE CURRENT RETRIEVAL AGAINST HBM MODEL. FOUR COMBINATIONS OF TWO DOPPLER MODELS, USED FOR WAVE REMOVAL, AND TWO WIND INPUTS TO THIS MODEL.

Doppler model	Wind input	Acquisition 1			Acquisition 2			Acquisition 3			Acquisition 4		
		Bias	RMSE	R	Bias	RMSE	R	Bias	RMSE	R	Bias	RMSE	R
DOPLUT-X	HIRLAM	0.124	0.137	0.876	-0.358	0.395	0.814	0.013	0.088	0.828	0.133	0.147	0.733
DOPLUT-X	XMOD2	0.108	0.124	0.853	-0.289	0.335	0.791	0.027	0.110	0.762	0.042	0.075	0.725
CDOP-X	HIRLAM	0.073	0.090	0.902	-0.299	0.344	0.825	-0.060	0.109	0.805	0.080	0.099	0.730
CDOP-X	XMOD2	0.065	0.084	0.895	-0.260	0.311	0.827	-0.036	0.111	0.751	0.024	0.062	0.744

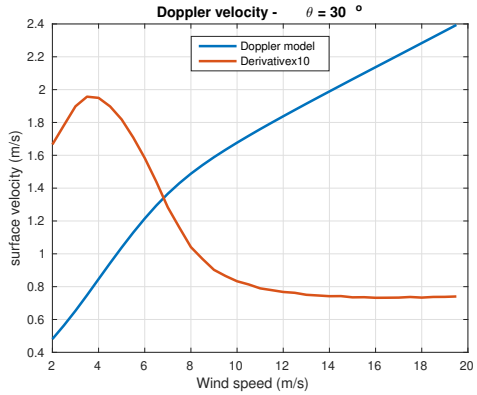

Fig. 11. Doppler velocity simulated using DOPLUT-X and its derivative as a function of wind speed for a given wind direction and incidence angle; blue curve: velocity, red curve: derivative $\times$ 10, for better visibility.

section V, was applied to all the acquisitions. Similarly, in all analysed images, the wind-wave induced phase was dominant even at relatively low wind speeds ($\sim$4-5 m/s). The sign of the phase before wave correction agrees with the wind direction and the magnitude is higher than expected from currents. Thus, wave correction as described in section VI was also applied to all the acquisitions.

For validation, the data having coherence below 0.2 and above 0.9 are filtered out. The lower value is because the phase information is not reliable and the higher value to remove targets in the water such as ships. The coherence filter is reinforced with a backscatter filter. So pixels with NRCS lower or larger than the response of the XMOD2 GMF to a wind speed of 2 and 15 m/s respectively are filtered. The filtered targets, which are not captured by the land mask but unlikely to be water, do not affect the HBM model. Moreover, values of surface currents larger than 2 m/s are also filtered out since they are unrealistic in this study area. Apart from these filters, no filtering of outliers was applied. Finally, the satellite measurements are resampled to the HBM model grid resolution.

Several differences are expected from the comparison of the SAR measurements against an ocean circulation model. First, the model surface current corresponds to the average of the upper (2 m) layer. The microwave radar measurements correspond literally to the surface. Second, due to large difference in the spatial resolution (few kms versus few meters), small scale oceanic features are not resolved by the model. Third, the Stokes drift, not taken into account by the model, is measured by SAR. This is still a matter of debate, see for instance [38], [39] for HF radar. Although most of the targets in the water, e.g. ships, have been filtered by the upper bounds of the coherence and backscatter restrictions, their wakes which are not filtered affect the surface roughness. These wakes might extend over several kilometres and their effects can be clearly

seen in SAR images. Finally, SAR measurements are very sensitive to bathymetry variation in shallow waters, which seems to have less effect on the model. This is mainly due to the coarse resolution of the bathymetric maps used by the models.

Figure 12 shows the residual velocity derived from TanDEM-X data after wave bias removal (first column), the HBM current field (second column) and their comparison (third column) for the four acquisitions. The similarity in the spatial variation is remarkable, though as expected, the model fields are smoother in contrast to the SAR fields that exhibit higher variability. The variations are not noise but geophysical variation not resolved by the model. Qualitatively, there is a good agreement (R>0.75) in the spatial gradients and direction of the currents between ATI-SAR and the ocean model. Both, for instance, clearly represent the accelerated inflows and outflows around the northern and southern islands in the channel. This indicates that the phase calibration and the wind-wave bias removal reveals the underlying current field. The wave induced velocity which is supposed to follow the quasi-uniform wind direction (see figure 3), is slowly varying in all images while the current field exhibits a high spatial variation as is observed in figure 12, first and second column.

Note that the scatter plots shown in the right column of figure 12 were obtained after a wind adjustment. This is done to minimise the bias in order to appreciate the spatial correlation with the same velocity scale. The wind speed is adjusted (for the wave correction) iteratively until the mean bias between the HBM model and retrievals is minimum. The Doppler model is sensitive to both wind speed and direction. It is however easier to adjust one control parameter than two and additionally the wind speed exhibits little spatial variation over the test area. Therefore, only a global wind speed offset is added or subtracted from the wind input to the Doppler model. The applied wind corrections are reported in the caption of figure 12 for each acquisition. The maximum wind offset correction is 5 m/s for study case 2, which records also the highest wind speed ($\sim 10\ m/s$) where the DOPLUT sensitivity is the lowest. Note that the maximum wind error resulting from our assessment (see figure 10) did not exceed 3 m/s in any case. Thus, this is an indication that DOPLUT might be biased. It should be noted that although called wind adjustment, it absorbs the wind bias and the Doppler model bias. It is difficult to separate these two components.

We assessed the wave bias removal using two different Doppler models (DOPLUT-X and CDOP-X) and two wind sources (DMI-HIRLAM and TerraSAR-X). The velocity bias, between the retrievals and the ocean model, after wave correction for the four study cases is reported in table IV. The bias is small (<0.13 m/s) except for the second acquisition, where it exceeds 0.2 m/s, which is the worst case in terms of bias and RMSE. This acquisition records the highest wind speed, sea level gradient (see section IX-B), current speed and strongest bathymetric modulations (see section IX-C). This higher RMSE of the second case is not due to the method precision, but to a locally spatial mismatch between the model and the retrieval. Thus it is rather a shortcoming of the HBM model which does not resolve the two strong (negative) jets around the northern island. Finally, if we assume a required current speed accuracy of 0.1 m/s, the obtained RMSE is comparable to the retrieval requirement except for the second case, which can not be validated with a coarse model.

B. Sea level effect

The Mean Sea Level (MSL) is provided hourly by the HBM model and by the two SMHI tide gauges Viken and Skanör (see figure 2 for their locations). The measurements are interpolated at the time of the satellite acquisition. The MSL records are depicted in figure 13. The model and in-situ measurements agree in the MSL variation for the four acquisitions. There is an absolute bias between the two sources, which is known [25], but this does not affect our interpretation. By comparing these curves with the retrieved current velocity (figure 12), one can observe a clear correlation between the sea level gradient and the current direction. Study cases 1, 3 and 4 have negative South-North MSL gradient which agrees with the southerly current and study case 2 have a positive gradient which agrees with the northerly current.

The circulation in the Öresund channel is often assumed to be dominated by the barotropic flow driven by the sea level difference between the Baltic Sea and the North Sea [21], [22], [31]. In fact both the model and retrieved currents in the four study cases agree in strength and direction with sea level gradient provided by the HBM model and in-situ measurements. For instance, acquisition 2 records the highest current speed (figure 12), and the sea level difference is $\sim$ 50 cm from north to the south of the scene ($\sim$ 50 km). However, our data sample (four acquisitions) is too small to validate such assumption. The total current is a combination of sea-level driven, wind drift and density-driven. A quantitative separation of the individual contributions of these components is beyond the scope of this paper. More frequent ATI-SAR acquisitions would be a valuable source of information for oceanographers to study such process.

C. Bathymetry effect

Bathymetry plays an important role in shaping the current path and modulating its strength [60]. Visual analysis of the derived velocity maps and the bathymetric maps explains a lot of current patterns which are not resolved by the HBM model. The bathymetry of the Öresund channel, provided by EMODnet (http://www.emodnet-bathymetry.eu/), is shown in figure 14. This figure is to be compared with the radial velocity maps shown in figure 12. The effect of bathymetry on the flow steering and acceleration is more obvious in the second study case. Many of these features are not visible in the model velocity field. For instance, the flow coming from the north is steered to the left (away from the radar) by the bathymetric channels around the northern island, hence the negative radial component while in the model map it is positive. The latter effect contributes to increase the negative bias found for this acquisition. Finally, it is known that SAR intensity images are affected by the bottom topography [47], [61]. Thus, velocity maps derived from ATI-SAR can be a good complement to SAR intensity images for researchers interested in retrieving bathymetry from SAR images.

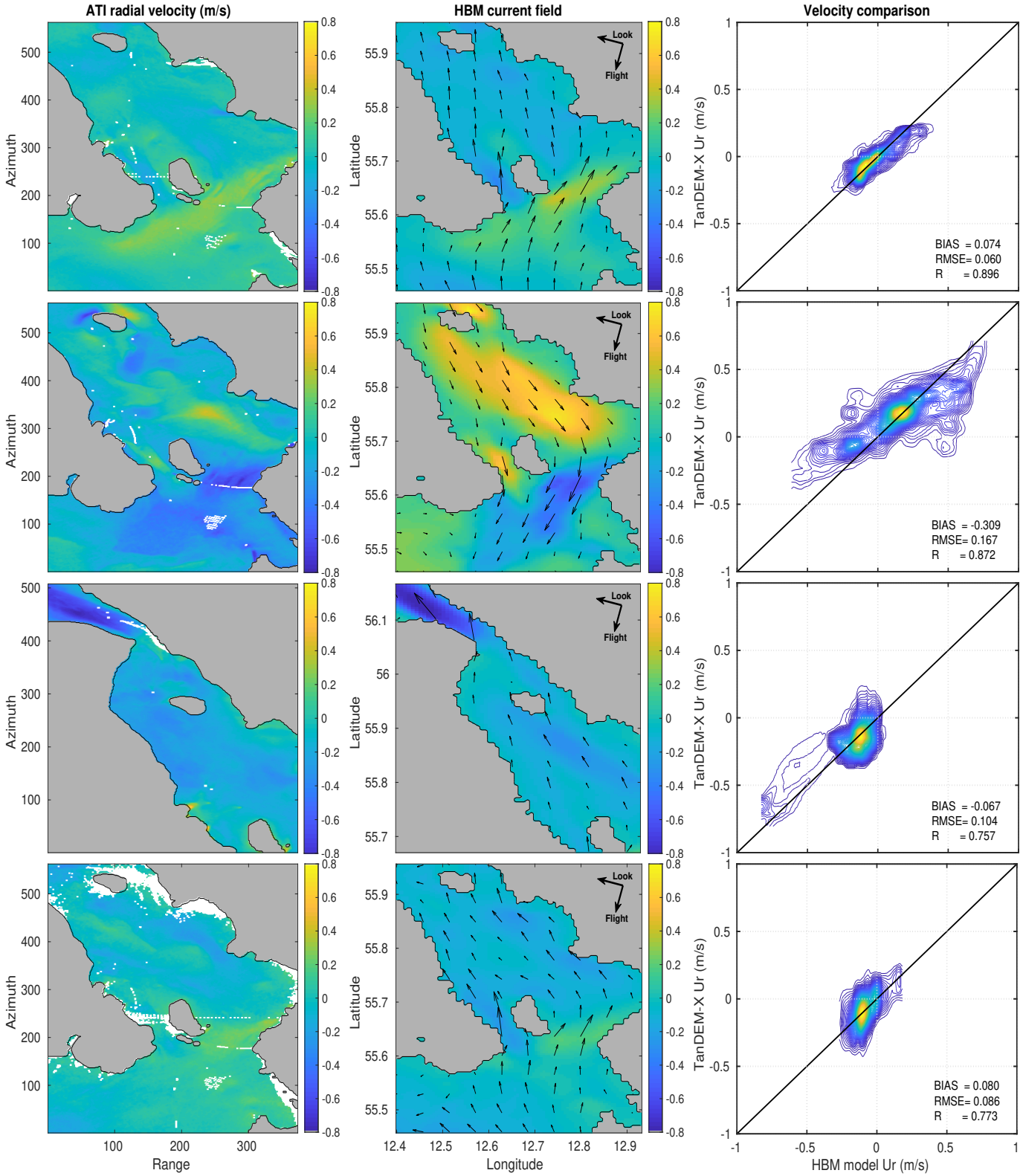

Fig. 12. Comparison of the ATI-SAR surface currents against the HBM model currents. Left column: TanDEM-X radial surface velocity after wave correction. The grey coloured area is land, the white pixels over sea are pixels filtered using coherence and backscatter limits (see text for more details); middle column: HBM model surface currents. The colour map is the model current vector projected on the SAR LOS and the arrows are the full current vector; right column: comparison TanDEM-X vs HBM. The colour in the scatter plot represents the density; First row: acquisition 2014-08-09 (wind correction -1.5 m/s); second row: acquisition 2014-08-20 (wind correction -5 m/s); third row: acquisition 2014-09-05 (wind correction -0.5 m/s); fourth row: acquisition 2014-09-11 (wind correction -1 m/s). The Root-Mean-Squared-Error (RMSE), the mean bias (BIAS) and the correlation coefficient (R) are shown in the scatter plots.

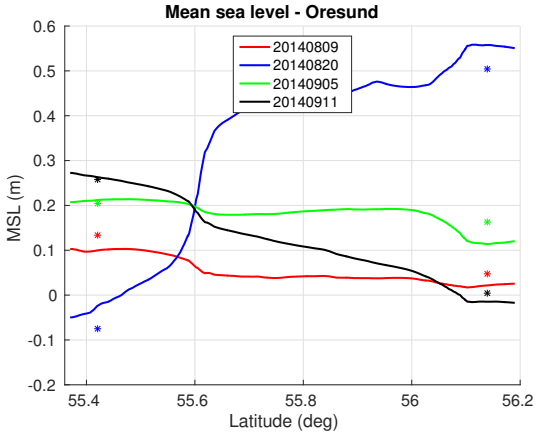

Fig. 13. Mean sea level variation for the four study cases obtained from HBM model, averaged over longitude across the Öresund channel. The stars are the in-situ measurements at the two SMHI stations Skanör and Viken (see map in figure 2 for locations).

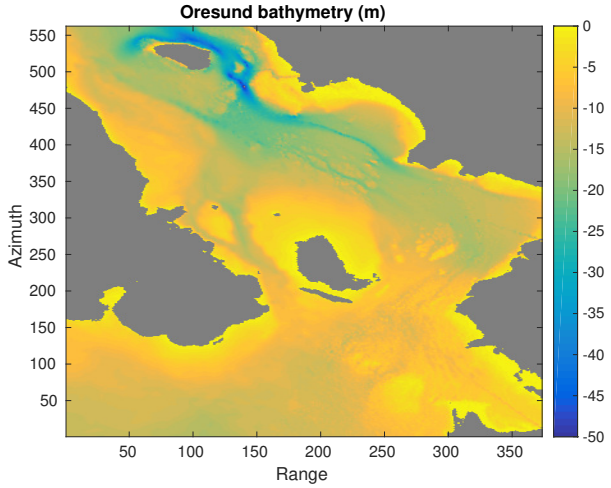

Fig. 14. Bathymetry of the Öresund channel, obtained from EMODnet (http://www.emodnet-bathymetry.eu), grey colour is land (height>0).

X. Conclusions

We analysed four interferograms based on SAR images acquired by the bistatic and hybrid system TanDEM-X over the Öresund channel located in the south-western Baltic Sea region. After removal of the across-track topography-dependent component, we found systematic ATI phase offsets in the processed interferograms. This can not be an artefact induced by the used DEM for the topographic correction since the same DEM applied to the same geographical area gives different offsets. This offset might be a combination of orbital errors, differences between the master and the slave electronic channels which induce different time delays and differences in the satellite attitudes. A calibration method, based on DInSAR to correct this phase offset, is proposed. The advantage of the proposed method is that it is not sensitive to the DEM absolute error as long as it does not exceed the HOA. Moreover, the method can be easily automatized, i.e. the land detection in the image and the topographic correction can be performed without need of human expertise. Moreover, exploiting all the land pixels provides an accurate estimate of the offset and allows an estimate of the phase standard deviation for performance assessment.

The wind-wave motion was the dominant contribution to the interferometric phase in the studied cases, even in relatively low wind conditions. This is also because the current speeds in the study areas are relatively low in general. Thus, wind-wave removal will always be needed in ocean current retrieval. This requires a Doppler model which relates the wind to Doppler shift induced by the surface waves and wind information. We assessed the wave correction using two different Doppler models (DOPLUT-X and CDOP-X) and two wind sources (DMI-HIRLAM and TerraSAR-X). The results of comparison of the retrieved currents against the ocean model HBM are provided in table IV. It is shown that the current retrieval is sensitive to the used Doppler model and wind source. The lowest bias and RMSE are obtained using CDOP-X as a Doppler model and the SAR wind speed as a wind source. The largest improvement (between the worst and best case) due to the use of CDOP-X instead of DOPLUT-X and SAR wind instead of HIRLAM is 44% and 30% in bias and RMSE respectively. This shows that using wind speed derived from the SAR backscatter not only allows an independent retrieval but also improves the current retrieval. The average improvement due to the use of CDOP-X model and SAR wind has roughly the same magnitude, i.e. 20% and 15% in bias and RMSE respectively. This is in agreement with our rough predictions in section VIII-A.

The phase uncertainty was derived empirically from data over land, after topography removal, and is shown in table III. The phase uncertainty is under 0.07 rad in all cases, hence it is not an obstacle for ATI-SAR measurements. The absolute phase offset can be corrected for as long as land is available. The Doppler model and wind errors have also been assessed. It was shown that the ATI-SAR current retrieval is sensitive to the Doppler model, wave spectrum and wind inaccuracies as discussed in section VIII-A. A current retrieval accuracy $\leq$ 0.1 m/s requires Doppler and wind errors σ_{f_D} <3.2 Hz and $\sigma_{U_{10}}$ <1 m/s respectively, at X-band and $\theta = 30^o$. Therefore, future systems measuring wind vectors, wave spectra and currents at the same time should alleviate this problem.

Though affected by uncertainties (phase noise, Doppler model and wind), it has been shown that the retrieval of ocean surface currents, provided a phase calibration and wave bias removal, yields good results compared to the ocean model even in areas with complex current patterns. The main advantage of using ATI systems for surface currents measurements is the high spatial resolution ($\approx$100 m), which is more than 10 times finer than existing ocean circulation models.

Acknowledgement

This work was financially supported by the Swedish National Space Board (contract dnr 167/14). Data from TerraSAR-X and TanDEM-X were provided by the German Aerospace Center (DLR) under the license agreement ATI OCEA0401. HBM model data were provided by the Danish Meteorological Institute (DMI). The authors would like to thank DLR and DMI. We would also like to thank our

colleagues Maciej Soja and Lars Jonasson for their support in TanDEM-X processing and the interpretation of HBM model data respectively.

REFERENCES

[1] V. Kudryavtsev, D. Akimov, J. A. Johannessen, and B. Chapron, "On radar imaging of current features: 1. model and comparison with observations," *Journal of Geophysical Research: Oceans*, vol. 110, no. C7, 2005.

[2] J. A. Johannessen, V. Kudryavtsev, D. Akimov, T. Eldevik, N. Winther, and B. Chapron, "On radar imaging of current features: 2. mesoscale eddy and current front detection," *Journal of Geophysical Research: Oceans*, vol. 110, no. C7, 2005.

[3] D. R. Thompson and J. R. Jensen, "Synthetic aperture radar interferometry applied to ship generated internal waves in the 1989 Loch Linnhe experiment," *Journal of Geophysical Research: Oceans*, vol. 98, no. C6, pp. 10 259–10 269, 1993.

[4] R. Romeiser and D. R. Thompson, "Numerical study on the along-track interferometric radar imaging mechanism of oceanic surface currents," *IEEE Transactions on Geoscience and Remote Sensing. Vol. 38-II, 446-458, 2000.*, vol. 38, no. 2, pp. 446–458, Jan 2000.

[5] J. A. Johannessen, R. A. Shuchman, G. Digranes, D. R. Lyzenga, C. Wackerman, O. M. Johannessen, and P. W. Vachon, "Coastal ocean fronts and eddies imaged with ERS-1 synthetic aperture radar," *Journal of Geophysical Research: Oceans*, vol. 101, no. C3, pp. 6651–6667, 1996.

[6] R. Goldstein and H. Zebker, "Interferometric radar measurement of ocean surface currents," *Nature*, vol. 328, pp. 707–709, 1987.

[7] R. Goldstein, H. Zebker, and T. P. Barnett, "Remote sensing of ocean currents," *Science*, vol. 246, pp. 1282–1285, September 1989.

[8] H. C. Graber, D. R. Thompson, and R. E. Carande, "Ocean surface features and currents measured with synthetic aperture radar interferometry and HF radar," *Journal of Geophysical Research*, vol. 101, no. C11, pp. 25 813–25 832, November 1996.

[9] R. Siegmund, M. Bao, S. Lehner, and R. Mayerle, "First demonstration of surface currents imaged by hybrid along- and cross-track interferometric SAR," *IEEE Transactions on Geoscience and Remote Sensing*, vol. 42, no. 3, pp. 511–519, March 2004.

[10] R. Romeiser, "Current measurements by airborne along-track InSAR: Measuring technique and experimental results," *IEEE Journal of Oceanic Engineering*, vol. 30, no. 3, pp. 552–568, July 2005.

[11] A. C. Martin and C. Gommenginger, "Towards wide-swath high-resolution mapping of total ocean surface current vectors from space: Airborne proof-of-concept and validation," *Remote Sensing of Environment*, vol. 197, pp. 58 – 71, 2017.

[12] R. Romeiser, H. Breit, M. Eineder, H. Runge, P. Flament, K. de Jong, and J. Vogelzang, "Current measurements by SAR along-track interferometry from a space shuttle," *IEEE Transactions on Geoscience and Remote Sensing*, vol. 43, no. 10, pp. 2315–2324, Sep 2005.

[13] R. Romeiser, S. Suchandt, H. Runge, S. Ulrich, and S. Grunler, "First analysis of TerraSAR-X along-track InSAR-derived current fields," *IEEE Transactions on Geoscience and Remote Sensing*, vol. 48, no. 2, pp. 820–829, Feb 2010.

[14] R. Romeiser, H. Runge, S. Suchandt, R. K. C. Rossi, and P. S. Bell, "Quality assessment of surface current fields from TerraSAR-X and TanDEM-X along-track interferometry and Doppler Centroid Analysis," *IEEE Transactions on Geoscience and Remote Sensing. Vol. 38-II, 446-458, 2000.*, vol. 52, no. 5, pp. 2759–2772, may 2014.

[15] S. Suchandt and H. Runge, "Ocean surface observations using the TanDEM-X satellite formation," *IEEE Journal of Selected Topics in Applied Earth Observations and Remote Sensing*, vol. 8, no. 11, pp. 5096–5105, Nov 2015.

[16] G. Krieger, A. Moreira, H. Fiedler, I. Hajnsek, M. Werner, M. Younis, and M. Zink, "TanDEM-X: A satellite formation for high-resolution SAR interferometry," *IEEE Transactions on Geoscience and Remote Sensing*, vol. 45, no. 11, pp. 3317–3341, Nov 2007.

[17] M. Leppranta and K. Myrberg, *Physical Oceanography of the Baltic Sea*, 1st ed. Springer, 2009.

[18] R. F. Hanssen, *Radar Interferometry: Data Interpretation and Error Analysis*, 1st ed. Springer, 2001.

[19] M. B. Kanevsky, *Radar Imaging of the Ocean Waves*. Elsevier, 2009.

[20] R. Feistel, G. Nausch, and N. Wasmund, *State and Evolution of the Baltic Sea, 19522005: A Detailed 50Year Survey of Meteorology and Climate, Physics, Chemistry, Biology, and Marine Environment*, 1st ed. Wiley, March 2008.

[21] J. Mattsson, "Observed linear flow resistance in the Öresund due to rotation," *Journal of Geophysical Research: Oceans*, vol. 100, no. C10, pp. 20 779–20 791, 1995.

[22] ——, "Some comments on the barotropic flow through the danish straits and the division of the flow between the belt sea and the Öresund," *Tellus A*, vol. 48, no. 3, pp. 456–464, 1996.

[23] R. Romeiser and H. Runge, "Theoretical evaluation of several possible along-track InSAR modes of TerraSAR-X for ocean current measurements," *IEEE Transactions on Geoscience and Remote Sensing*, vol. 45, no. 1, pp. 21–35, Jan 2007.

[24] P. Berg and J. W. Poulsen, "Implementation details for HBM," DMI, Tech. Rep., 2012.

[25] I. Golbecka, S. Jandt, I. Lorkowski, P. Lagemaa, T. Brning, V. Huess, A. Hartman, and S. Verjovkina, "Baltic Sea physical analysis and forecasting product baltic SEA_ANALYSIS_FORECAST_PHY_003_006," Copernicus: Marine environment monitoring service, Tech. Rep., 2018.

[26] S. Duque, "TanDEM-X Payload Ground Segment - CoSSC Generation and Interferometric Considerations," DLR, Tech. Rep., May 2012.

[27] E. Rodriguez and J. M. Martin, "Theory and design of interferometric synthetic aperture radars," *IEE Proceedings F - Radar and Signal Processing*, vol. 139, no. 2, pp. 147–159, April 1992.

[28] J. V. Toporkov, P. A. Hwang, M. A. Sletten, G. Farquharson, D. Perkovic, and S. J. Frasier, "Surface velocity profiles in a vessels turbulent wake observed by a dual-beam along-track interferometric SAR," *IEEE Transactions on Geoscience and Remote Sensing Letters*, vol. 8, no. 4, pp. 602–606, jul 2011.

[29] T. L. Ainsworth, S. R. Chubb, R. A. Fusina, R. M. Goldstein, R. W. Jansen, J.-S. Lee, and G. R. Valenzuela, "INSAR imagery of surface currents, wave fields, and fronts," *IEEE Transactions on Geoscience and Remote Sensing*, vol. 33, no. 5, pp. 1117–1123, sep 1995.

[30] D. Massonnet, M. Rossi, C. Carmona, F. Adragna, G. Peltzer, K. Feigl, and T. Rabaute, "The displacement field of the Landers earthquake mapped by radar interferometry," *Nature*, vol. 364, p. 138142, July 1993.

[31] F. Wulff, L. Rahm, and P. Larsson, *A Systems Analysis of the Baltic Sea*, 1st ed. Springer, 2001.

[32] D. R. Thompson, *Calculation of Microwave Doppler Spectra from the Ocean Surface with a Time-Dependent Composite Model*. Dordrecht: Springer Netherlands, 1989, pp. 27–40.

[33] D. R. Thompson, B. L. Gotwols, and W. C. Keller, "A comparison of Ku-band Doppler measurements at 20^o incidence with predictions from a time dependent scattering model," *Journal of Geophysical Research: Oceans*, vol. 96, no. C3, pp. 4947–4955.

[34] B. Chapron, F. Collard, and F. Ardhuin, "Direct measurements of ocean surface velocity from space: Interpretation and validation," *Journal of Geophysical Research*, vol. 110, 2005.

[35] C. Gelpi and K. Norris, "Estimated surface-wave contributions to radar Doppler velocitymeasurements of the ocean surface," *Remote Sensing of Environment.*, vol. 87, pp. 99–110, June 2003.

[36] A. C. H. Martin, C. Gommenginger, J. Marquez, S. Doody, V. Navarro, and C. Buck, "Wind-wave-induced velocity in ATI-SAR ocean surface currents: First experimental evidence from an airborne campaign," *Journal of Geophysical Research: Oceans*, vol. 121, no. 3, 2016.

[37] G. Broström, K. H. Christensen, and J. E. H. Weber, "A quasi-eulerian, quasi-lagrangian view of surface-wave-induced flow in the ocean," *Journal of Physical Oceanography*, vol. 38, no. 5, pp. 1122–1130, 2008.

[38] F. Ardhuin, L. Mari, N. Rascle, P. Forget, and A. Roland, "Observation and estimation of Lagrangian, Stokes, and Eulerian currents induced by wind and waves at the sea surface," *Journal of Physical Oceanography*, vol. 39, no. 11, pp. 2820–2838, 2009.

[39] J. Röhrs, A. K. Sperrevik, K. H. Christensen, G. Broström, and Ø. Breivik, "Comparison of HF radar measurements with Eulerian and Lagrangian surface currents," *Ocean Dynamics*, vol. 65, no. 5, pp. 679–690, May 2015.

[40] J. A. Johannessen, B. Chapron, F. Collard, V. Kudryavtsev, A. Mouche, D. Akimov, and K. Dagestad, "Direct ocean surface velocity measurements from space: Improved quantitative interpretation of Envisat ASAR observations," *Geophysical Research Letters*, vol. 35, no. 22, 2008.

[41] N. Rascle, F. Ardhuin, P. Queffeulou, and D. Croiz-Fillon, "A global wave parameter database for geophysical applications. part 1: Wave-currentturbulence interaction parameters for the open ocean based on traditional parameterizations," *Ocean Modelling*, vol. 25, no. 3, pp. 154 – 171, 2008.

[42] A. Mouche, B. Chapron, N. Reul, and F. Collard, "Predicted Doppler shifts induced by ocean surface wave displacements using asymptotic electromagnetic wave scattering theories," *Waves in Random and Complex Media*, vol. 18, no. 1, pp. 185–196, 2008.

[43] F. Fois, P. Hoogeboom, F. L. Chevalier, and A. Stoffelen, "An analytical model for the description of the fullpolarimetric sea surface Doppler signature," *Journal of Geophysical Research: Oceans*, vol. 120, no. 2, pp. 988–1015, 2015.

[44] F. Said, H. Johnsen, B. Chapron, and G. Engen, "An ocean wind Doppler model based on the generalized curvature ocean surface scattering model," *IEEE Transactions on Geoscience and Remote Sensing*, vol. 53, no. 12, pp. 6632–6638, Dec 2015.

[45] J. W. Wright, W. J. Plant, W. C. Keller, and W. L. Jones, "Ocean wave-radar modulation transfer functions from the west coast experiment," *Journal of Geophysical Research: Oceans*, vol. 85, no. C9, pp. 4957–4966, 1980.

[46] F. Feindt, J. Schrter, and W. Alpers, "Measurement of the ocean wave radar modulation transfer function at 35 GHz from a seabased platform in the North Sea," *Journal of Geophysical Research: Oceans*, vol. 91, no. C8, pp. 9701–9708, 1986.

[47] R. Romeiser, W. Alpers, and V. Wismann, "An improved composite surface model for the radar backscatter cross section of the ocean surface, 1. theory of the model and optimization / validation by scatterometer data," *Journal of Geophysical Research*, vol. 102, no. C11, pp. 25 237–25 250, Nov 1997.

[48] A. Mouche, F. Collard, B. Chapron, K. Dagestad, G. Guitton, J. A. Johannessen, V. Kerbaol, and M. Hansen, "On the use of Doppler shift for sea surface wind retrieval from SAR," *IEEE Transactions on Geoscience and Remote Sensing*, vol. 50, no. 7, pp. 2901–2909, Jul 2012.

[49] A. C. Martin, C. P. Gommenginger, and Y. Quilfen, "Simultaneous ocean surface current and wind vectors retrieval with squinted sar interferometry: Geophysical inversion and performance assessment," *Remote Sensing of Environment*, vol. 216, pp. 798 – 808, 2018.

[50] V. Kudryavtsev and J. Johannessen, "On effect of wave breaking on short wind waves," *Geophysical Research Letters*, vol. 31, no. 20, October 2004.

[51] M. Hansen, V. Kudryavtsev, B. Chapron, J. Johannessen, F. Collard, K.-F. Dagestad, and A. Mouche, "Simulation of radar backscatter and Doppler shifts of wave current interaction in the presence of strong tidal current," *Remote Sensing of Environment*, vol. 120, pp. 113 – 122, 2012.

[52] A. A. Mouche, D. Hauser, and V. Kudryavtsev, "Radar scattering of the ocean surface and sea-roughness properties: A combined analysis from dual-polarizations airborne radar observations and models in C-band," *Journal of Geophysical Research: Oceans*, vol. 111, no. C9, 2006.

[53] W. Koch, "Directional analysis of SAR images aiming at wind direction," *IEEE Transactions on Geoscience and Remote Sensing*, vol. 42, no. 4, pp. 702–710, 2004.

[54] G. K. Carvajal, L. E. B. Eriksson, and L. M. H. Ulander, "Retrieval and quality assessment of wind velocity vectors on the ocean with C-band SAR," *IEEE Transactions on Geoscience and Remote Sensing*, vol. 52, no. 5, pp. 2519–2537, 2014.

[55] X. M. Li and S. Lehner, "Algorithm for sea surface wind retrieval from TerraSAR-X and TanDEM-X data," *IEEE Transactions on Geoscience and Remote Sensing*, vol. 52, no. 5, pp. 2928–2938, May 2014.

[56] H. Johnsen, V. Nilsen, G. Engen, A. A. Mouche, and F. Collard, "Ocean Doppler anomaly and ocean surface current from Sentinel-1 TOPS mode," in *2016 IEEE International Geoscience and Remote Sensing Symposium (IGARSS)*, July 2016, pp. 3993–3996.

[57] T. Elfouhaily, B. Chapron, K. Katsaros, and D. Vandemark, "A unified directional spectrum for long and short wind-driven waves," *Journal of Geophysical Research: Oceans*, vol. 102, no. C7, pp. 15 781–15 796, 1997.

[58] M. W. Hansen, F. Collard, K. F. Dagestad, J. A. Johannessen, P. Fabry, and B. Chapron, "Retrieval of sea surface range velocities from Envisat ASAR Doppler centroid measurements," *IEEE Transactions on Geoscience and Remote Sensing*, vol. 49, no. 10, pp. 3582–3592, Oct 2011.

[59] A. Bentamy, D. Croize-Fillon, , and C. Perigaud, "Characterization of ASCAT measurements based on buoy and QuikSCAT wind vector observations," *Ocean Science,*, vol. 4, no. 4, pp. 265–274, November 2008.

[60] S. T. Gille, E. J. Metzger, and R. Tokmakian, "Seafloor topography and ocean circulation," *Oceanography*, vol. 17, March 2004.

[61] W. Alpers and I. Hennings, "A theory of the imaging mechanism of underwater bottom topography by real and synthetic aperture radar," *Journal of Geophysical Research: Oceans*, vol. 89, no. C6, pp. 10 529–10 546, 1984.

Anis Elyouncha Anis Elyouncha (S'18) received the B.S. degree in Electrical engineering from the Institut Superieur Industriel de Bruxelles, Brussels, Belgium, in 2004, the M.S. degree in electrical engineering and telecommunications from the Universite Libre de Bruxelles, Brussels, Belgium, in 2006. From 2008 to 2015 he was a research engineer in the Royal Military Academy of Belgium. Now he is a PhD student in the department of Space Earth and Environment at Chalmers university of Technology, Gothenburg, Sweden. His research interests include ocean parameters retrieval from SAR data, electromagnetic scattering from the sea surface and radar signal processing.

Leif E. B. Eriksson Leif E. B. Eriksson (M05) received a University Certificate in Space Technology from Ume University, Umeå, Sweden in 1993, the M.S. degree in electrical engineering from Chalmers University of Technology, Gothenburg, Sweden, in 1998, and the Ph.D. degree from Friedrich-Schiller University, Jena, Germany, in 2004. From 1999 to 2000 he was employed by the Joint Research Centre of the European Commission at the Space Application Institute in Ispra, Italy, Between 2000 and 2004 he was with the Department of Geoinformatics at the Friedrich-Schiller University in Jena, Germany, In 2004 he joined the radar remote sensing group at Chalmers University of Technology, Gothenburg, Sweden, where he since 2012 holds a position as Associate Professor in radar remote sensing, currently at the Department of Space, Earth and Environment. His research interests include the use of SAR to retrieve information about ocean, sea ice and forest.

Roland Romeiser (M00SM13) received the Dipl.-Phys. degree from the University of Bremen, Germany, in 1990 and the Dr.rer.nat. and Habilitation degrees from the University of Hamburg, Germany, in 1993 and 2007, respectively. From 1990 to 2008, he was a Project Scientist / permanent Staff Scientist with the Institute of Oceanography, University of Hamburg. From August 1998 to July 1999, he spent a year at the Applied Physics Laboratory, Johns Hopkins University, Laurel, Maryland, USA, as a Feodor Lynen Fellow of the Alexander von Humboldt Foundation. In April 2008, he became an Associate Professor with the Rosenstiel School of Marine and Atmospheric Science of the University of Miami, Florida, USA, where he is now a full Professor. He has wide experience in the field of remote sensing of ocean currents, waves, and winds by airborne and spaceborne microwave radars. Most of his recent research has focused on advanced synthetic aperture radar (SAR) processing and algorithm development for current and wave retrievals. Dr. Romeiser has been an Associate Editor of the IEEE Journal of Oceanic Engineering since fall 2000 and was an Associate Editor of the IEEE Transactions on Geoscience and Remote Sensing from 2014 to 2017.

Lars M. H. Ulander Lars M. H. Ulander (S86-M90-SM04-F17) received the M.Sc. degree in engineering physics and the Ph.D. degree in electrical and computer engineering from Chalmers University of Technology, Gothenburg, Sweden, in 1985 and 1991, respectively. Since 2014, he is Professor in radar remote sensing at Chalmers University of Technology. He also holds a part-time position at the Swedish Defence Research Agency (FOI), Linköping, where he is Director of Research in radar signal processing and leads the research on VHF/UHF-band radar. His research areas include synthetic aperture radar (SAR), signal processing, electromagnetic scattering models and remote sensing applications. He is author or co-author of over 300 professional publications, of which more than 70 are in peer-reviewed scientific journals.